Characterization of tumor angiogenesis in rat brain using Iron-based Vessel Size Index MRI in combination with Gadolinium-based Dynamic Contrast Enhanced MRI

Marine Beaumont, PhD[1,2], Benjamin Lemasson, MSc[1,2,3], Régine Farion[1,2], Christoph Segebarth, PhD[1,2], Chantal Rémy, PhD[1,2], Emmanuel L. Barbier, PhD[1,2]

[1]Inserm, U836, Grenoble, F-38042, France

[2]Université Joseph Fourier, Grenoble Institut des Neurosciences, UMR-S836, Grenoble, F-38042, France

[3]Oncodesign Inc., 20, rue Jean Mazen BP 27627, F-21076 Dijon Cedex, France

Corresponding Author: Emmanuel Barbier

Grenoble Institut des Neurosciences (GIN)

Centre de Recherche INSERM U836 / Equipe 5

Université Joseph Fourier - Site Santé à La Tronche

BP 170

38042 Grenoble cedex 9

France

Tel.: +33 4 56 52 05 88

Fax: +33 4 56 52 05 98

Email: emmanuel.barbier@ujf-grenoble.fr

Acknowledgments: The authors thank the "Institut National du Cancer", the "Cancéropôle Lyon Auvergne Rhône-Alpes", the "Association pour la Recherche sur le Cancer" and the "Région Rhône-Alpes" for their financial support and Guerbet for providing Sinerem®. BL received a stipend from Oncodesign Inc.

Running headline: Combined VSI and DCE MRI

Word Count: 5696 (max. 6000)

ABSTRACT

This study aimed at combining an iron-based, steady-state, Vessel Size Index MRI approach (VSI MRI), and a Gd-based, Dynamic Contrast Enhanced MRI approach (DCE MRI) to characterize tumoral microvasculature. Rats bearing an orthotopic glioma (C6, n=14 and RG2, n=6) underwent DCE MRI and combined VSI and DCE MRI four hours later, at 2.35T. Gd-DOTA (200 µmol of Gd/kg) and ultrasmall superparamagnetic iron oxide (USPIO) (200 µmol of iron/kg) were used for DCE and VSI MRI, respectively. C6 and RG2 glioma were equally permeable to Gd-DOTA but presented different blood volume fractions and VSI, in good agreement with histological data. The presence of USPIO yielded reduced K^{trans} values. The K^{trans} values obtained with Gd-DOTA in absence and in presence of USPIO were well correlated for the C6 glioma but not for the RG2 glioma. It was also observed that, within the time frame of DCE MRI, USPIO remained intravascular in the C6 glioma while it extravasated in the RG2 glioma. In conclusion, VSI and DCE MRI can be combined provided that USPIO does not extravasate with the time frame of the DCE MRI experiment. The mechanisms at the origin of USPIO extravasation remain to be elucidated.

Key words: blood volume, dynamic contrast-enhanced MRI (DCE MRI), brain tumors, ultrasmall superparamagnetic iron oxide particles (USPIO), vessel size index (VSI).

INTRODUCTION

Assessing angiogenesis is of considerable interest when determining tumor grade and prognosis (Burger *et al* 1985; Daumas-Duport *et al* 1997). In clinical practice, angiogenesis is assessed in terms of microvessel density as determined on surgical biopsies (Takei *et al* 2007). This approach is limited by how accurately the biopsy can sample a highly heterogeneous vascular environment commonly found in high grade tumors. Necrotic areas exhibit sparse and degraded vessels, while angiogenic areas are characterized by high vessel density (Carmeliet and Jain 2000), large vessel diameters (Brown *et al* 2001), and increased permeability. *In vivo* imaging methods that enable non-invasive, 3D monitoring of microvasculature, therefore, present a major interest for tumor management (Hou *et al* 2006). Also, there is currently a strong need for imaging surrogate markers of angiogenesis (Gagner *et al* 2005).

Magnetic Resonance Imaging (MRI) is one of the most promising techniques to provide such markers. It is considered the method of choice for diagnosing brain tumors, providing information about tumor size and location, extent of edema, relative blood volume fraction (BVf), and blood-brain barrier (BBB) status. For characterization of brain microvasculature, the most widely used MRI method is dynamic susceptibility contrast (DSC) imaging. With this method, the first pass of an intravenous (IV) injected bolus of a gadolinium-based contrast agent (CA) is monitored (Barbier *et al* 2001). Then, information on blood volume, blood flow, vessel size, and CA arrival and transit times can be derived. If extravasation of the CA is monitored using dynamic contrast enhanced MRI (DCE MRI), the status of the BBB can be evaluated (Tofts *et al* 1999). With brain tumors, the accuracy of the parameters derived from DSC MRI may be affected due to alterations of the BBB (Schmainda *et al* 2004). Steady-state methods to characterize blood volume are an alternative to DSC MRI. They rely on the changes in the transverse relaxation times due to an intravascular iron-based CA (ultrasmall superparamagnetic iron oxide - USPIO) and do not require the estimation of the arterial input function (AIF). With this approach, it is possible to estimate BVf and to obtain information on the distribution of microvessel radii (Dennie *et al* 1998; Kiselev *et al* 2005; Pathak *et al* 2001; Schmainda *et al* 2004; Troprès *et al* 2004). The latter information – an approximation of the mean vessel radius – can be expressed in terms of vessel size index

(VSI, in μm) (Kiselev *et al* 2005; Troprès *et al* 2004). MRI mapping of VSI has been validated in various animal models (Ferretti *et al* 2005; Troprès *et al* 2004; Valable *et al* 2008). In humans, VSI and BVf have been mapped using gadolinium chelates rather than USPIO (Batchelor *et al* 2007; Kiselev *et al* 2005; Schmainda *et al* 2004).

Since steady-state MRI acquisitions do not require rapid temporal sampling, BVf and VSI maps can be obtained with high spatial resolution. Moreover, the steady-state approach does not require measuring the AIF, and it is relatively insensitive to alterations of the BBB. These features render the steady-state method particularly suited to characterizing microvasculature during tumor growth and to assessing the efficacy of anti-angiogenic and/or anti-vascular therapies in animals. However, the steady-state approach does not provide an estimate of the BBB permeability, a key parameter in brain tumor characterization and in monitoring therapeutic effects (Batchelor *et al* 2007; Gossmann *et al* 2002). We, therefore, addressed the question of whether or not we could combine a steady-state approach – to assess BVf and VSI using an iron-based CA – with a DCE MRI approach – to evaluate the BBB status using a Gd-based CA.

In designing this study, we had two objectives: i) To combine the two approaches into a single imaging protocol. ii) To assess to what extent the intravascular presence of an iron-based CA affects parameters derived from DCE MRI.

We evaluated two glioma models (C6 and RG2) using both the combined protocol (USPIO and Gd) and the DCE MRI-only protocol (Gd).

METHODS

Animal preparation

Experiments were performed under permits n° 380521 (for one of the researchers involved), A3851610004 (for the experimental facility) and B3851610003 (for the animal care facility) from the French Ministry of Agriculture. All experiments were performed under anesthesia with the following parameters: 5% isoflurane for induction, 2% for maintenance in 60% air / 40% oxygen. Rectal temperature was maintained at 37.0±0.5°C throughout the experiments using a water blanket.

C6 and RG2 glioma models were used as orthotopic brain tumor models. Male Wistar rats (175-200 g, n = 14) for the C6 model and male Fischer 344 rats (150-175 g, n = 6) for the RG2 model were placed onto a stereotactic head holder and a scalp incision was performed along the median line. A 1 mm diameter burr hole was drilled in the skull, 3 mm laterally to Bregma. A 5 µl cell suspension [1.10^5 C6 cells (ATCC, CCL-107) or 5.10^3 RG2 cells (ATCC, CRL-223) in phosphate buffered saline complemented with 2% of glutamine and 1% of penicillin streptomycin] was injected in 5 min into the right caudate nucleus, at a depth of 6 mm under the skull, using a Hamilton syringe. The needle was slowly removed 5 minutes after the injection and the burr hole was plugged with vegetal wax. Mean survival times were 28±5 and 22±3 days for the C6 and RG2 models, respectively (Valable *et al* 2008).

For each imaging session, a catheter was inserted into the tail vein for CA administration. At the end of the second imaging session (*cf. MRI*), each animal was euthanized and the brain was excised and frozen for histological study.

MRI

Experiments were performed on a 2.35 T, 40 cm diameter horizontal bore magnet (Bruker, Wissenbourg, France) equipped with a 20 cm diameter actively shielded gradient system (Magnex Scientific Ltd, Oxford, UK) and interfaced with a SMIS console (SMIS Ltd, Guildford, UK). Maximum gradient strength and slew rate were 96 mT/m and 128 T/m/s, respectively. The MR probes (RAPID Biomedical GmbH, Rimpar, Germany) consisted in a volume coil for emission and a surface coil for reception. Both

coils were linearly polarized; they were both geometrically and actively decoupled. Each imaging session started with tumor localization, using a T_2-weighted spin-echo sequence (TR/TE = 2000/80 ms, field of view (FOV) = 30 mm, matrix = 256 x 192, 19 slices, slice thickness (ST) = 1 mm). The slice containing the largest homogeneous tumor (i.e. without necrotic cores to avoid Gd-DOTA encapsulation) area was selected for imaging with ensuing sequences.

Experiment A: Does the presence of USPIO affect DCE MRI estimates?

The plasmatic half life of Gd-DOTA (~30 min in rats) is significantly shorter than that of USPIO (~4h30 min in rats). If DCE MRI were performed before BVf/VSI MRI, the intravascular and tissular concentrations of Gd-DOTA would not be stable enough during the 25min-long BVf/VSI protocol. Conversely, the plasmatic concentration of USPIO can be considered stable during the realization of a 30min long DCE MRI protocol. Thus, in the combined protocol, the BVf/VSI measurements were performed prior to the DCE measurements.

Each animal was imaged twice a day, 14 days after tumor implantation. During the first session, only the DCE MRI protocol was performed. During the second session, the animal underwent first the BVf/VSI protocol and then the DCE MRI protocol (combined protocol, Figure 1). A 4 hour delay between the two imaging sessions allowed clearance from the tumor of the Gd-DOTA injected during the first session (Fonchy *et al* 2001).

Steady-state BVf/VSI MRI

For the steady-state approach, we used USPIO (Sinerem®, Guerbet, France / Combidex®, AMAG Pharmaceuticals, Inc, USA; diameter 30 nm, longitudinal relaxivity $r_1 = 8\ mM^{-1}.s^{-1}$, transversal relaxivity $r_2 = 89\ mM^{-1}.s^{-1}$ (37°C and 2.35T)). As in previous studies, a multi gradient-echo and spin-echo MRI sequence (TR = 6 s, 7 evenly spaced gradient-echoes (GE) = [6-42] ms, 1 spin-echo = 102 ms, voxel size = 234 x 454 x 2000 μm^3) was acquired just prior to and 3 min after manual administration of USPIO (200 µmoles of iron/kg body weight, via the tail vein in about 20 sec) (Troprès *et al* 2004; Valable *et al* 2008).

DCE MRI

For the DCE MRI, we used a low molecular weight Gd-based CA, Gd-DOTA (Dotarem®, Guerbet, France; diameter 1nm, r_1 = 3.4 $mM^{-1}.s^{-1}$ (37°C and 2.35T)). A baseline T_1 map was derived from variable density spiral (VDS) measurements (Kim *et al* 2003) performed at different delays from a preparation inversion pulse (11 inversion times (TI), TR/TE = 4400/1.6 ms, flip angle = 90°, acquisition time per interleaf (T_{acq}) = 11.7 ms, 5 interleaves, FOV = 30 mm, matrix = 64 x 64, ST = 2 mm). Then, a set of T_1-weighted (T_1w) images were acquired sequentially using a VDS sequence (TR/TE = 600/1.6 ms, flip angle = 90°, T_{acq} = 10.4 ms, 16 interleaves, FOV = 30 mm, matrix = 128 x 128, ST = 2 mm). After the acquisition of 5 baseline images, a long bolus of Gd-DOTA was administered into the tail vein (200 µmoles of Gd/kg, 12 mL/h, entire dose injected within 30 s for a 250 g rat). Images were sampled every 9.6 s during the initial 5 min and every 19.2 s subsequently (time span covered: 32 min).

Experiment B: Does USPIO remain intravascular during the DCE MRI protocol?

To evaluate whether the USPIO remained intravascular over the time span of the combined protocol, a DCE MRI-like experiment was performed on four additional animals (2 C6 and 2 RG2 bearing animals were imaged 18 and 14 days after tumor implantation, respectively). The DCE MRI protocol was applied as described above (acquisition of a baseline T_1 map followed by a set of T_1w images), but the overall time span covered was extended to 120 min. After the acquisition of 5 T_1w baseline images, USPIO (200 µmoles of iron/kg body weight) was injected similarly as the Gd-DOTA.

Histology

Frozen brain tissue was cut with a cryostat (ST = 10 µm). Five coronal slices were generated per animal. After fixing in methanol/acetone (50% v/v) and washing in tap water for 5 min, one slice was stained with hematoxylin-erythrosin (HE, nucleus and cytoplasm staining, respectively). Two slices were used for highlighting vessel and blood brain barrier (BBB) integrity, using type IV collagen (against basal lamina)

and Rat Blood-Brain Barrier antibodies (i.e. against an endothelial protein found in areas with blood-brain or blood nerve barriers), respectively. Slices were rehydrated in phosphate-buffered saline (PBS, 0.01M) and fixed in 4% paraformaldehyde. After saturation in PBS-Tween 0.01%-BSA 3% for 30 min at room temperature, a goat antibody against collagen IV (Southern Biotech, Birmingham, AL, ref. 1340-01, 1/2000) and a mouse antibody against rat BBB (Covance, Princeton, NJ, ref. SMI 71R, 1/500) were incubated overnight at 4°C in PBS-Tween 0.01%-BSA 1%. Revelation used an Alexa 546-linked Donkey anti goat IgG (Invitrogen, Cergy Pontoise, France, ref. A11030, 1/200) and an Alexa 488 linked Donkey antimouse IgG (Invitrogen, Cergy Pontoise, France, ref. A21202, 1/200). The last two slices were labeled with ED1 (AbCys, Paris, France, ref AbC117-6714, 1/2000), an antibody directed against a membrane receptor CD68 present on rat macrophage lysosomal membrane. Nucleus counterstaining was performed using DAPI.

Data processing

All operations described in this section were performed on a pixel-wise basis using in-house programs developed in Matlab 7 (The MathWorks, Inc, Natick, NA). Pixels with an intensity below 5% of the image maximum (on raw data) were excluded from the processing. Note that this threshold was used to remove background pixels. All pixels originating from tissues of interest were kept in the analysis. All model fitting procedures (for T_2*, T_1 and pharmacokinetic parameters determination) used a Levenberg-Marquardt algorithm.

BVf/VSI experiment

T_2^* was computed from the 7 GE images acquired before ($T_{2\,before}^*$) and after ($T_{2\,after}^*$) USPIO injection by fitting a monoexponential function to the signal decay. Then, $\Delta R_2^* = 1/T_{2\,after}^* - 1/T_{2\,before}^*$ was calculated. ΔR_2 was derived from the two spin-echo signals, acquired before (S_{before}) and after (S_{after}) USPIO injection:

$$\Delta R_2 = \frac{1}{TE} \ln\left(\frac{S_{before}}{S_{after}}\right). \quad [1]$$

BVf and VSI were obtained as described by Troprès *et al*. (Troprès *et al* 2004):

$$\begin{cases} BVf = \dfrac{3}{4\pi} \dfrac{\Delta R_2^*}{\gamma \Delta\chi B_0} \\ VSI = 0.424 \left(\dfrac{ADC}{\gamma \Delta\chi B_0}\right)^{1/2} \left(\dfrac{\Delta R_2^*}{\Delta R_2}\right)^{3/2} \end{cases}, \quad [2]$$

where γ is the gyromagnetic ratio, B_0 is the static magnetic field, $\Delta\chi$ is the increase in blood magnetic susceptibility due to the USPIO, and ADC is the apparent diffusion coefficient of water. We used $\Delta\chi = 0.57\ 10^{-6}$ CGS units and ADC = 720 $\mu m^2/s$ for RG2 tumor, muscle and contralateral cerebral tissue and ADC = 974 $\mu m^2/s$ for C6 tumor (data previously measured in similar experimental conditions (Valable *et al* 2008)).

DCE MRI

VDS MR data were first corrected for non-idealities of the spiral k-space trajectories (Beaumont *et al* 2007). They were then interpolated onto a cartesian grid (128 x 128) using linear gridding and zero filling, where appropriate. T_{10} (reference T_1 value) was estimated by fitting the following model function to the data:

$$M(TI) = M_0 (1 - 2\, c \exp(-TI/T_{10})), \quad [3]$$

where M_0, c and T_{10} are the adjustable parameters to be estimated. M(TI) is the signal at inversion time TI, M_0 is the equilibrium signal, and c is a constant accounting for non-idealities of the inversion pulse. T_1w signal intensities S were converted into T_1 values using:

$$T_1 = -TR / \ln(1 - S/S_0), \quad [4]$$

where S_0 is the fully relaxed MR signal intensity. S_0 was obtained from the baseline signal intensity ($S_{baseline}$) and T_{10}:

$$S_0 = S_{baseline} / \left(1 - e^{-TR/T_{10}}\right). \quad [5]$$

Gd-induced changes ΔR_1 (i.e. $1/T_1$-$1/T_{10}$) were converted into Gd concentrations ([Gd]), using the Gd-DOTA relaxivity r_1 measured in water (we made the approximation that r_1 was constant in the different tissues):

$$[Gd] = \Delta R_1 / r_1 . \quad [6]$$

Data from Experiment B (DCE MRI using USPIO) were processed similarly, but they were not converted into CA concentrations. Thus, only USPIO-induced changes ΔR_1 values were obtained in this case.

To derive pharmacokinetic parameters from Experiment A (Gd-based DCE MRI), an AIF is required. Due to the loss of linearity between MR signal and CA concentration at high concentration values, and due to partial volume effect, we were not able to obtain the AIF directly from the DCE MRI data. We used a reference AIF based on arterial blood sampling, as previously determined in the laboratory. The reference AIF increases linearly (tracer injection as a long bolus) and then decays biexponentially (tracer clearance). The reference AIF, or $C_p(t)$, is fully characterized by the following equation:

$$\begin{cases} C_p(t) = 0, \text{ when } 0 \le t \le t_A \\ C_p(t) = \dfrac{A_1 + A_2}{t_P - t_A}(t - t_A), \text{ when } t_A < t \le t_P , \\ C_p(t) = A_1 e^{-tB_1} + A_2 e^{-tB_2}, \text{ when } t_P < t \end{cases} \quad [7]$$

where t_A and t_P are the arrival time and the time to peak, respectively. The amplitudes are $A_1 = 1.94$ mM and $A_2 = 0.76$ mM, and the time constants are $B_1 = 1.01$ min^{-1} and $B_2 = 0.03$ min^{-1}. t_A and t_P were estimated for each rat and each DCE MRI experiment using an automated procedure.

DCE MRI pharmacokinetic parameters were estimated by fitting the model function $C_t(t)$ to the evolution of [Gd] over time (Tofts *et al* 1999):

$$C_t(t) = v_p C_p(t) + K^{trans} \int_0^t C_p(\tau)\, e^{-(t-\tau)k_{ep}} d\tau . \quad [8]$$

where v_p (plasma volume fraction), K^{trans} (volume transfer constant between blood plasma and extravascular extracellular space (EES)) and k_{ep} (flux rate constant between EES and plasma) were the adjustable parameters. Then, v_e (EES volume fraction) was calculated:

$$v_e = K^{trans}/k_{ep} . \quad [9]$$

Note that although BVf and v_p both represent the plasma volume fraction, they arise from two different physiological model.

Histology

Histological data from twelve animals (6 C6 and 6 RG2; other brains were not available) were quantitatively analyzed. Sections (up to 3 fields of view per ROI and per slice, three slices/animal) were digitized using a CCD camera (Olympus, Rungis, France). Collagen IV images were binarized (threshold manually defined) and vascular parameters [mean vessel density, fractional vascular surface (VSurf), mean vessel radius (r) and mean vessel length (h)] were obtained using ImageJ software (Rasband, W.S., ImageJ). To allow comparison between MR data and histological data, VSI_{histo} was derived from 2D slices as described in (Troprès *et al* 2004) and BVf_{histo} was computed as described in (Pathak *et al* 2001):

$$BVf_{histo} = \left(\frac{rh}{rh + (r+h)ST} \right) \left[-2\ln(1 - VSurf) \right] \times 100 , \quad [10]$$

where ST is the section thickness.

Data analysis

For each DCE MRI experiment, two ROIs were manually drawn on the [Gd] map: tumor and temporal muscle. These two ROIs were reported on BVf and VSI maps. For the analysis of these two last parameters, a third ROI was drawn on the contralateral brain tissue.

Within each ROI, pixels presenting estimates outside predefined ranges were excluded from ROI analyses. For BVf and VSI, the conditions of validity (0-15% and 0-50 µm, respectively) are those

defined in (Valable *et al* 2008) – our data were collected in identical experimental conditions – and they derive from the theoretical framework behind the MRI method (Troprès *et al* 2004). We further required T_1 to be positive and v_p, v_e, K^{trans} and k_{ep} to be positive and smaller than 1. For each ROI, mean and standard error of the mean (SEM) were calculated for each parameter.

Statistical analysis was based on the permutation test, which is suited to data originating from small and different sized groups, and with unknown distributions (Pitman 1937). Unpaired permutation tests were applied to compare the two tumor models. To compare values between ROIs or between experiments performed on the same animal, paired permutation tests were used. All statistical analyses were performed with Matlab 7. DCE MRI pharmacokinetic parameters estimated in the absence and presence of USPIO are indicated USPIO- and USPIO+, respectively.

RESULTS

Experiment A – MR images

Figure 1 shows typical examples of MR images acquired on two rats, one for each tumor model. For both models, the signal of the tumor on the T_1w-image enhances as soon as 5 min after Gd-DOTA injection (Figure 1D and N). The tumors are also visible on T_2-weigthed images as hyperintense regions (Figure 1A, E, K and O).

In the C6 model, the USPIO induced a moderate decrease of the overall GE and SPIRAL signal intensities, with hypointense vessels, both in contralateral and tumor tissues (Figure 1G, I and J). In the RG2 tumor, the GE signal decrease after USPIO injection was more pronounced than in the C6 tumor and its T_1w-SPIRAL signal was slightly enhanced at the periphery, even before Gd-DPTA injection, suggesting an extravasation of USPIO (Figure 1Q, S and T). After injection of USPIO and of Gd-DOTA, signal enhancement due to Gd-DOTA extravasation can readily be detected in both tumor models (Figure 1J and T). However, signal increase dropped from 58% to 44% in the C6 model and from 65% to 23% in the RG2 model. Note that in the contralateral rat brain, T_1 decreased by about 8% after injection of USPIO (data not shown).

Experiment A – Gd concentration time curves

Figure 2 presents examples of Gd concentration-time curves and their fits. On each graph, temporal evolutions of one representative pixel from the tumor ROI and one pixel from the muscle ROI are plotted. The top row shows the evolution of the concentration time curves for the Wistar model between the two DCE MRI experiments, before (left) and after (right) USPIO injection; the Fischer model is presented on the bottom row. Displayed curves are representative of the all rats for each model. All temporal evolutions were successfully fitted by the model (Eq. [8]). In the muscle, Gd concentration-time curves showed a similar CA uptake pattern, for both models. The presence of USPIO did not strongly modify this pattern, only the wash-out process (decreasing part of the curve) seemed slower. In the tumor, the two models exhibited different CA uptake curves. Before USPIO injection, the CA uptake in the RG2 tumor

followed a “vascular” pattern while in the C6 tumor, the Gd concentration reached its maximum well after the initial bolus phase. After USPIO injection, the temporal evolution in the C6 tumor was very similar to that obtained in absence of USPIO whereas in the RG2, the Gd concentration-time curve was strongly modified.

Experiment A: Wistar model – C6 tumor versus Fischer model – RG2 tumor

Figure 3 shows the quantitative results of the DCE MRI USPIO- (Session 1) and the BVf/VSI (Session 2) experiments for each animal model. All values are reported in Table 1. Temporal muscle as well as contralateral brain tissue presented comparable BVf and VSI values in both rat strains. BVf and v_p in the RG2 tumor (BVf = 4.5±0.3%; v_p = 1.8±0.2%) were about twice as large as in the C6 tumor (BVf = 2.8±0.1%; v_p = 0.9±0.1%), which had a BVf similar to that in contralateral tissue (BVf = 2.4±0.1%). BVf was larger than v_p in tumor while the converse was true in temporal muscle. VSI was larger in the C6 (14.4±1.5 µm) than in the RG2 tumor (8.7±0.7 µm), and both were larger than that in contralateral brain tissue (5.1±0.3 µm). v_e was larger in the C6 than in the RG2 tumor and in both tumor types, it was larger than in temporal muscle. K^{trans} in the C6 and in the RG2 tumors was comparable to that in temporal muscle. k_{ep} was lower in the C6 than in the RG2 tumor, and in both tumor types, k_{ep} was lower than in temporal muscle.

Experiment A: USPIO+ experiment versus USPIO- experiment

Pharmacokinetic parameters estimated in the USPIO- condition (Session 1) and in the USPIO+ condition (Session 2) are compared on Figure 4 and values reported in Table 1. Because no significant difference was found in parameters estimated in the muscle between Wistar and Fischer rats (Figure 3), results from both animal models were pooled for the muscle ROI. For the C6 tumor and the muscle, all the pharmacokinetic parameter values determined in the presence of USPIO were slightly lower than the ones determined in the absence of USPIO. However, the paired statistical tests did not reveal statistical differences between the parameter values measured before and after the USPIO injection, except for

K^{trans}. For the RG2 model, the pharmacokinetic parameters estimated in the tumor region were significantly reduced by the presence of USPIO. The only exception was for the parameter v_e, which presented a higher value in the USPIO+ condition than in the USPIO- condition. However, one has to bear in mind that v_e is calculated for each animal and for each pixel of the ROI as the ratio of K^{trans} and k_{ep} and, thus, is not an independent parameter.

Experiment B

As mentioned in the Methods section, the DCE MRI data obtained using USPIO as CA (Experiment B) were converted into ΔR_1 to enable comparison with the data obtained using Gd-DOTA. Figure 5 shows the temporal evolution of ΔR_1 obtained in three ROIs, on four rats. ΔR_1 in muscle and in contralateral brain evolved similarly in both animal models. Upon bolus arrival, ΔR_1 increased in muscle and remained stable afterwards. In contralateral brain tissue, ΔR_1 slightly decreased upon bolus arrival and remained stable afterwards. In the RG2 tumor, ΔR_1 remained stable for a few minutes and increased continuously afterwards. No plateau was reached during the two-hour acquisition time window. The two RG2 rats presented different rates of signal increase, likely due to the different amounts of CA injected. In the C6 model, R_1 remained unchanged over the same period of time.

Histology

For both tumor models, HE stained brain sections showed that cellular density was larger in the tumor than contralaterally. Neither macroscopic necrotic regions nor hemorrhage were observed. In C6 tumor, Collagen IV labeling showed lower vessel density and higher vessel diameter compared to contralateral brain tissue (Figure 6A-B). Similar differences, but less pronounced, were found in the RG2 tumor (Figure 6C-D). For both tumor types, BBB labeling was much lower in the tumor centre than contralaterally (Figure 6E-H). Finally, the level of ED1 labeling (macrophages) seemed higher in the centre of the RG2 tumor than in the C6 tumor, while it was almost totally absent in the contralateral brain

tissue (Figure 6I-L). Results of the quantitative analysis of the histological data are reported on Table 1. Both tumor models presented a lower vessel density in the tumor than in the contralateral brain tissue. BVf_{histo} measured in the RG2 tumor was larger than the one in the C6 tumor, which was comparable to the BVf_{histo} value in contralateral brain tissue. VSI_{histo} was not different between the two tumor models but was found significantly higher than in the contralateral brain tissue.

DISCUSSION

This study shows that a DCE MRI experiment can be combined within the same MRI session to a steady-state BVf/VSI measurement protocol, provided that USPIO does not extravasate. K^{trans} values obtained with the combined protocol are 20% smaller than those obtained with a DCE MRI protocol alone. However, when USPIO does not extravasate (i.e. in the C6 model), K^{trans} estimates are well correlated with K^{trans} values calculated from the data obtained without the combined USPIO/Gd protocol. Physiological information obtained from the DCE MRI experiment and that from the steady-state MRI experiment are complementary, improving the characterization of the microvasculature in glioma models. All MR results were in good agreement with histological observations.

In muscle, BVf and v_p estimates were comparable (mean for all 20 animals are 1.8±0.1% and 2.1±0.7%, respectively) and in good agreement with values from the literature (Everett *et al* 1956; Schwarzbauer *et al* 1993). In contralateral brain tissue, BVf estimates were comparable to previously published data obtained with the same method (Troprès *et al* 2004; Valable *et al* 2008). In tumor, blood volume as assessed by BVf, BVf_{histo} and v_p was twice as large in the RG2 model than in the C6 model. BVf estimates (steady-state MRI approach) were larger than histological estimates (BVf_{histo}) and both were larger than v_p estimates (DCE MRI approach). Although BVf and v_p estimates were different, they were well correlated in the tumor (R^2 = 0.70). As discussed by Valable *et al.* (Valable *et al* 2008), BVf estimated with the steady-state MRI approach or the histology are prone to various source of bias. Quantitative histological estimates suffer sampling errors due to cryosectioning and from 2D to 3D extrapolation errors (Pathak *et al* 2001). The steady-state MRI approach may be biased by macroscopic magnetic field inhomogeneities and by limitations of the underlying theoretical model (Pathak *et al* 2008). DCE MRI estimates are very sensitive to the AIF (Port *et al* 2001) and to the choice of the physiological model. An underestimation of the parameter v_p can arise from various sources, as shown in (Cheng 2008), including inaccurate AIF measurements, limited temporal resolution, and transit time effects. The shutter speed effect (Li *et al* 2005) may also play a determinant role in the estimation of v_p. However, in our protocol, the CA was injected as a long bolus, which may reduce the shutter speed

influence on v_p. Covariance between model parameters is another factor which may bias v_p estimate (Buckley 2002). Further investigation is required to understand why BVf and v_p provide different estimates of the plasma volume fraction.

The VSI results were in good agreement with estimates obtained under similar experimental conditions (Valable *et al* 2008). Histological and MR estimates of VSI are biased by the same factors as those described above for BVf. Additionally, non-ideal Collagen labeling yields an apparent vessel fragmentation in the sections. The subsequent analysis thus produces more and smaller vessels which eventually yields an underestimation of VSI_{histo}. This could explain both the small estimates of VSI obtained by histology and the lack of difference between VSI_{histo} measured in C6 and RG2 tumors in this study. The fact that the C6 model presents a higher VSI value together with a smaller BVf value than the RG2 model is consistent with a reduction in vessel density more marked in the C6 than in the RG2 tumor and suggested by our histological results.

Mean estimates of K^{trans} and v_e in muscle were 0.019±0.001 min^{-1} and 7.4±0.7%, respectively, in good agreement with estimates from peri-prostate muscle tissue (K^{trans}=0.015 min^{-1} and v_e=8%) (Kershaw and Buckley 2006). In both of our tumor models, BBB alterations were detected by DCE MRI and histology. This is consistent with a previous study (Valable *et al* 2008) which indicated that vascular endothelial growth factor (VEGF) is equally overexpressed in C6 and RG2 tumors. While pharmacokinetic estimates were in good agreement with the literature (Ferrier *et al* 2007), we did not find a significant difference in K^{trans} (measured in the absence of USPIO) between the two models (there is however a trend towards a larger K^{trans} in the C6 model), in contrast to a previous observation (Uehara *et al* 1997). This discrepancy could be related to differences between the two studies in the perfusion status of the animals (e.g. due to anesthesia). Indeed, K^{trans} is sensitive to different parameters: blood flow (in $ml.g^{-1}.min^{-1}$), the surface vessel wall (in $cm^2.g^{-1}$), the actual permeability of the capillary wall (in $cm.min^{-1}$) (Tofts *et al* 1999) and possibly by CA diffusion into the extravascular extracellular space and water exchange (Li *et al* 2005). Moreover, since C6 and RG2 tumors present different vessel densities and blood volumes (Valable *et al*

2008), they are not likely to present identical surfaces of vessel wall. Thus, while K^{trans} may be similar among tumor types as reported in this study, the actual permeability of C6 and of RG2 tumor vessels may differ.

All parameter estimates obtained from the DCE MRI experiment were reduced by the USPIO. This reduction was significant for RG2 tumor only and very weak for C6 tumor and muscle tissue. This reduction may be explained in terms of magnetic field gradients generated within and around the vessels. Even at the short TE (1.6 ms) used in this study, these gradients reduce the MR signal intensities from within the vessels and from their periphery. The signal reduction from blood explains a lower v_p value estimated in the presence of USPIO. The reduction of the contribution of the vessel periphery to the signal might explain the decrease in the three other parameter values, v_e, K^{trans} and k_{ep} observed in the presence of USPIO, assuming limited diffusion of Gd-DOTA across the EES at the periphery of vessels. Transendothelial water exchange may also have contributed to the reduction observed in pharmacokinetic parameters (Li *et al* 2005). Moreover, the apparent CA relaxivity in the voxel (r_1) may also have been affected by the presence of USPIO (Li *et al* 2005). It would be of interest to evaluate how the diffusion of CA in EES and the water exchanges (transendothelial and transcytolemmal) affect the estimates obtained in USPIO+ condition, using an adapted modeling of the different signal contributions in the presence of USPIO. The presence of the magnetic field gradients, induced by the USPIO, not only reduces the signal intensity in the surrounding tissue but also may invalidate the two-compartment DCE model (i.e. extended Tofts model) since the field gradient extending into the extravascular space will make the assumption of a single extravascular compartment questionable. Despite a significant effect of the USPIO on the estimate of K^{trans}, a strong correlation between this estimate and that obtained from a combined protocol was found in the C6 model ($R^2 = 0.78$). The coefficient of determination R^2 was lower for the RG2 tumor ($R^2 = 0.41$) than for the C6 tumor, likely due to the different extravasation properties of the USPIO in the two models – no extravasation in the C6 tumor, slow extravasation in the RG2 tumor (up to 2 hours after injection). Also, this phenomenon probably explains why the presence of USPIO

significantly reduced all the estimates determined in the RG2 model. Because USPIO is present in intra- and extravascular compartments, the effects of water diffusion and of water exchanges through the different membranes on the pharmacokinetic parameters estimates may be emphasized and lead to a strong reduction of these estimates. Following this hypothesis, one can suggest to lower the dose of USPIO and thus decrease the impact of the presence of iron on the estimates of K^{trans}. However, a lower dose may affect the plasmatic half-life of the USPIO and impair the steady-state hypothesis for the DCE MRI experiment. Also, it has been shown (Troprès *et al* 2004) that a high dose is necessary to provide accurate VSI measurements across the entire vessel size spectrum. Finally, the parameter v_e has to be considered with caution as it is not determined independently.

It is unclear which features underlie the difference in USPIO extravasation between the two tumor models. Three mechanisms can be considered. (i) Passive diffusion, the mechanism at the origin of Gd-DOTA extravasation. This study shows that both tumor models are equally permeable to Gd-DOTA and present similar histological BBB labeling. However, as mentioned above, the two tumors present different ADC values. Thus, a difference in EES interstitial pressure could prevent USPIO from extravasating in the C6 tumor but not in the RG2 tumor. (ii) Active transport via macrophages (Corot *et al* 2004; Saleh *et al* 2004). This assumption is supported by our histological results, which show a macrophage labeling more pronounced in the RG2 tumor than in the C6 tumor. This assumption is, however, not supported by the timing of the USPIO extravasation. It began a few minutes after CA arrival and was, thus, too fast to allow time for macrophagic capture and transport across the vessel wall (Daldrup *et al* 1999). (iii) Active transport via endothelial cells. Pinocytic activity in endothelial cells is known to be significantly higher in glioma than in healthy brain tissue and can contribute to the extravasation of CA (Shivers *et al* 1984; Takano *et al* 1991). In contrast to the macrophage response, a transport via pinocytic vesicles could occur within minutes after CA injection (Nag *et al* 1981; Petito 1979). A combination of these three mechanisms may also explain the reported extravasation of USPIO. Understanding this extravasation requires further investigation, such as determining how the observed phenomenon depends on the CA

size. A detailed understanding of the mechanisms involved in USPIO extravasation could provide a new way of characterizing tumors.

CONCLUSION

This study shows that an iron-based BVf/VSI MRI experiment and a Gd-based DCE MRI experiment can be combined into a unique MRI protocol, provided that USPIO does not extravasate with the time frame of the DCE MRI experiment. In this case, the combined protocol proposed in this study appears well suited for evaluating anti-angiogenic therapies: blood volume fraction, vessel size (and thus vessel density), and vessel permeability can be estimated within a single MRI session, as was successfully done on the C6 glioma model. The behavior of the RG2 model indicates that this protocol cannot be used on every tumor model, however. Beyond the fact that such a combined protocol enriches the set of quantitative microvascular parameters, additional microvascular characteristics may emerge from this approach – an adapted modeling of the different signal contributions in the presence of USPIO and Gd-DOTA might provide insights into the diffusion of Gd-DOTA within the EES and/or on water exchange through cell membrane. Finally, USPIO extravasation may be used to differentiate tumor models that are indistinguishable based on Gd-DOTA permeability like C6 and RG2 models.

REFERENCES

Barbier EL, Lamalle L, Decorps M (2001) Methodology of brain perfusion imaging. *J Magn Reson Imaging* 13:496-520.

Batchelor TT, Sorensen AG, di TE, Zhang WT, Duda DG, Cohen KS, Kozak KR, Cahill DP, Chen PJ, Zhu M, Ancukiewicz M, Mrugala MM, Plotkin S, Drappatz J, Louis DN, Ivy P, Scadden DT, Benner T, Loeffler JS, Wen PY, Jain RK (2007) AZD2171, a pan-VEGF receptor tyrosine kinase inhibitor, normalizes tumor vasculature and alleviates edema in glioblastoma patients. *Cancer Cell* 11:83-95.

Beaumont M, Lamalle L, Segebarth C, Barbier EL (2007) Improved *k*-space trajectory measurement with signal shifting. *Magn Reson Med* 58:200-5.

Brown EB, Campbell RB, Tsuzuki Y, Xu L, Carmeliet P, Fukumura D, Jain RK (2001) In vivo measurement of gene expression, angiogenesis and physiological function in tumors using multiphoton laser scanning microscopy. *Nat Med* 7:864-8.

Buckley D, L. (2002) Uncertainty in the analysis of tracer kinetics using dynamic contrast-enhanced T_1-weighted MRI. *Magn Reson Med* 47:601-6.

Burger PC, Vogel FS, Green SB, Strike TA (1985) Glioblastoma multiforme and anaplastic astrocytoma. Pathologic criteria and prognostic implications. *Cancer* 56:1106-11.

Carmeliet P, Jain RK (2000) Angiogenesis in cancer and other diseases. *Nature* 407:249-57.

Cheng HL (2008) Investigation and optimization of parameter accuracy in dynamic contrast-enhanced MRI. *J Magn Reson Imaging* 28:736-43.

Corot C, Petry KG, Trivedi R, Saleh A, Jonkmanns C, Le Bas JF, Blezer E, Rausch M, Brochet B, Foster-Gareau P, Baleriaux D, Gaillard S, Dousset V (2004) Macrophage imaging in central nervous system and in carotid atherosclerotic plaque using ultrasmall superparamagnetic iron oxide in magnetic resonance imaging. *Invest Radiol* 39:619-25.

Daldrup HE, Link TM, Blasius S, Strozyk A, Könemann S, Jürgens H, Rummeny EJ (1999) Monitoring radiation-induced changes in bone marrow histopathology with ultra-small superparamagnetic iron oxide (USPIO)-enhanced MRI. *J Magn Reson Imaging* 9:643-52.

Daumas-Duport C, Varlet P, Tucker ML, Beuvon F, Cervera P, Chodkiewicz JP (1997) Oligodendrogliomas. Part I: Patterns of growth, histological diagnosis, clinical and imaging correlations: a study of 153 cases. *J Neurooncol* 34:37-59.

Dennie J, Mandeville JB, Boxerman JL, Packard SD, Rosen BR, Weisskoff RM (1998) NMR imaging of changes in vascular morphology due to tumor angiogenesis. *Magn Reson Med* 40:793-9.

Everett NB, Simmons B, Lasher EP (1956) Distribution of blood (Fe 59) and plasma (I 131) volumes of rats determined by liquid nitrogen freezing. *Circ Res* 4:419-24.

Ferretti S, Allegrini PR, O'Reilly T, Schnell C, Stumm M, Wartmann M, Wood J, McSheehy PM (2005) Patupilone induced vascular disruption in orthotopic rodent tumor models detected by magnetic resonance imaging and interstitial fluid pressure. *Clin Cancer Res* 11:7773-84.

Ferrier MC, Sarin H, Fung SH, Schatlo B, Pluta RM, Gupta SN, Choyke PL, Oldfield EH, Thomasson D, Butman JA (2007) Validation of dynamic contrast-enhanced magnetic resonance imaging-derived vascular permeability measurements using quantitative autoradiography in the RG2 rat brain tumor model. *Neoplasia* 9:546-55.

Fonchy E, Lahrech H, Francois-Joubert A, Dupeyre R, Benderbous S, Corot C, Farion R, Rubin C, Decorps M, Remy C (2001) A new gadolinium-based contrast agent for magnetic resonance imaging of brain tumors: kinetic study on a C6 rat glioma model. *J Magn Reson Imaging* 14:97-105.

Gagner JP, Law M, Fischer I, Newcomb EW, Zagzag D (2005) Angiogenesis in gliomas: imaging and experimental therapeutics. *Brain Pathol* 15:342-63.

Gossmann A, Helbich TH, Kuriyama N, Ostrowitzki S, Roberts TPL, Shames DM, van Bruggen N, Wendland MF, Brasch RC (2002) Dynamic contrast-enhanced magnetic resonance imaging as a surrogate marker of tumor response to anti-angiogenic therapy in a xenograft model of glioblastoma multiforme. *J Magn Reson Imaging* 15:233-40.

Hou LC, Veeravagu A, Hsu AR, Tse VC (2006) Recurrent glioblastoma multiforme: a review of natural history and management options. *Neurosurg Focus* 20:E5.

Kershaw LE, Buckley DL (2006) Precision in measurements of perfusion and microvascular permeability with T_1-weighted dynamic contrast-enhanced MRI. *Magn Reson Med* 56:986-92.

Kim DH, Adalsteinsson E, Spielman DM (2003) Simple analytic variable density spiral design. *Magnetic Resonance in Medicine* 50:214-9.

Kiselev VG, Strecker R, Ziyeh S, Speck O, Hennig J (2005) Vessel size imaging in humans. *Magn Reson Med* 53:553-63.

Li X, Huang W, Yankeelov TE, Tudorica A, Rooney WD, Springer CS, Jr. (2005) Shutter-speed analysis of contrast reagent bolus-tracking data: Preliminary observations in benign and malignant breast disease. *Magn Reson Med* 53:724-9.

Nag S, Robertson DM, Dinsdale HB (1981) Cerebrovascular permeability in mechanically induced hypertension. *Can J Neurol Sci* 8:215-20.

Pathak AP, Schmainda KM, Ward BD, Linderman JR, Rebro KJ, Greene AS (2001) MR-derived cerebral blood volume maps: issues regarding histological validation and assessment of tumor angiogenesis. *Magn Reson Med* 46:735-47.

Pathak AP, Ward BD, Schmainda KM (2008) A novel technique for modeling susceptibility-based contrast mechanisms for arbitrary microvascular geometries: the finite perturber method. *Neuroimage* 40:1130-43.

Petito CK (1979) Early and late mechanisms of increased vascular permeability following experimental cerebral infarction. *J Neuropathol Exp Neurol* 38:222-34.

Pitman EJG (1937) Significance Tests Which May be Applied to Samples From any Populations. *Suppl J R Statist Soc* 4:119-30.

Port RE, Knopp MV, Brix G (2001) Dynamic contrast-enhanced MRI using Gd-DTPA: interindividual variability of the arterial input function and consequences for the assessment of kinetics in tumors. *Magn Reson Med* 45:1030-8.

Saleh A, Wiedermann D, Schroeter M, Jonkmanns C, Jander S, Hoehn M (2004) Central nervous system inflammatory response after cerebral infarction as detected by magnetic resonance imaging. *NMR Biomed* 17:163-9.

Schmainda KM, Rand SD, Joseph AM, Lund R, Ward BD, Pathak AP, Ulmer JL, Badruddoja MA, Krouwer HG (2004) Characterization of a first-pass gradient-echo spin-echo method to predict brain tumor grade and angiogenesis. *AJNR Am J Neuroradiol* 25:1524-32.

Schwarzbauer C, Syha J, Haase A (1993) Quantification of regional blood volumes by rapid T1 mapping. *Magn Reson Med* 29:709-12.

Shivers RR, Edmonds CL, Del Maestro RF (1984) Microvascular permeability in induced astrocytomas and peritumor neuropil of rat brain. A high-voltage electron microscope-protein tracer study. *Acta Neuropathol* 64:192-202.

Takano S, Yoshii Y, Nose T (1991) [Ultrastructure of glioma vessel--morphometric study for vascular permeability]. *No To Shinkei* 43:49-56.

Takei H, Bhattacharjee MB, Rivera A, Dancer Y, Powell SZ (2007) New immunohistochemical markers in the evaluation of central nervous system tumors: a review of 7 selected adult and pediatric brain tumors. *Arch Pathol Lab Med* 131:234-41.

Tofts PS, Brix G, Buckley DL, Evelhoch JL, Henderson E, Knopp MV, Larsson HB, Lee TY, Mayr NA, Parker GJ, Port RE, Taylor J, Weisskoff RM (1999) Estimating kinetic parameters from dynamic contrast-enhanced T(1)-weighted MRI of a diffusable tracer: standardized quantities and symbols. *J Magn Reson Imaging* 10:223-32.

Troprès I, Lamalle L, Péoc'h M, Farion R, Usson Y, Décorps M, Rémy C (2004) In vivo assessment of tumoral angiogenesis. *Magn Reson Med* 51:533-41.

Uehara H, Miyagawa T, Tjuvajev J, Joshi R, Beattie B, Oku T, Finn R, Blasberg R (1997) Imaging experimental brain tumors with 1-aminocyclopentane carboxylic acid and alpha-aminoisobutyric acid: comparison to fluorodeoxyglucose and diethylenetriaminepentaacetic acid in morphologically defined tumor regions. *J Cereb Blood Flow Metab* 17:1239-53.

Valable S, Lemasson B, Farion R, Beaumont M, Segebarth C, Remy C, Barbier EL (2008) Assessment of blood volume, vessel size and the expression of angiogenic factors in two rat glioma models: a longitudinal *in vivo* and *ex vivo* study. *NMR in Biomedicine* 10:1043-56.

TITLES AND LEGENDS TO FIGURES AND TABLES:

Figure 1: Protocol combining a BVf/VSI experiment with a DCE MRI experiment and images obtained at each stage of the protocol.

The chronogram of MRI protocol for Experiment A is presented at the top of the figure. The names of the sequences, their respective TR, TE and durations, and the CA injections are indicated. Note that the MRI protocol of Session 1 is the same as the MRI protocol of Session 2 except that the two MGESE sequences and the injection of USPIO are missing. **(A-T)** examples of images obtained on one animal per tumor model using the MRI protocol of Experiment A, Sessions 1 (**A-D** for the C6 model and **K-N** for the RG2 model) and 2 (**E-J** for the C6 model and **O-T** for the RG2 model). Images acquired after CA injections are annotated with names of the CA injected and times post-injection in minutes.

Figure 2: Temporal evolution of [Gd]

Examples of temporal evolutions of [Gd] encountered during the DCE MRI analysis (**A** and **C**) in the USPIO- condition and (**B** and **D**) in the USPIO+ condition: tumor and muscle from (**A**-**B**) one animal bearing a C6 tumor and (**C**-**D**) one animal bearing a RG2 tumor. For each set of data points, the result of the fitting procedure is plotted (solid lines). Plots correspond to the time courses of a single pixel issued from the ROI.

Figure 3: BVf, VSI and DCE MRI pharmacokinetic parameter estimates in the C6 and RG2 models.

Parameters obtained in Experiment A (mean±SEM) for each tumor model (C6 in black and RG2 in gray) and different tissue ROIs. BVf and VSI were obtained during Session 2. v_p, v_e, K^{trans} and k_{ep} are the results of Session 1 (USPIO-).

Figure 4: DCE MRI pharmacokinetic parameter estimates obtained in presence or in absence of USPIO.

The pharmacokinetic parameters obtained in Session 1 (USPIO-, black) and in Session 2 (USPIO+, gray) are represented as mean±SEM. Data obtained in the muscle have been pooled across tumor models (n=20) while data from the C6 tumor and the RG2 tumor were kept separated (n=14 and n=6 respectively).

Figure 5: Does the USPIO extravasate in the tumor?

Temporal evolutions of the longitudinal relaxation rate after USPIO injection in Experiment B. Each graph corresponds to one ROI, and, in each graph, each time course was obtained from a single animal (four time courses per graph: 2 C6 (open symbols) and 2 RG2 (filled symbols)). Dashed lines and double arrows indicate the time at which MR acquisitions and Gd injection were performed during Experiment A, Session 2, prior and after USPIO injection (time = 0 min was defined as the beginning of the USPIO injection).

Figure 6: Histological images.

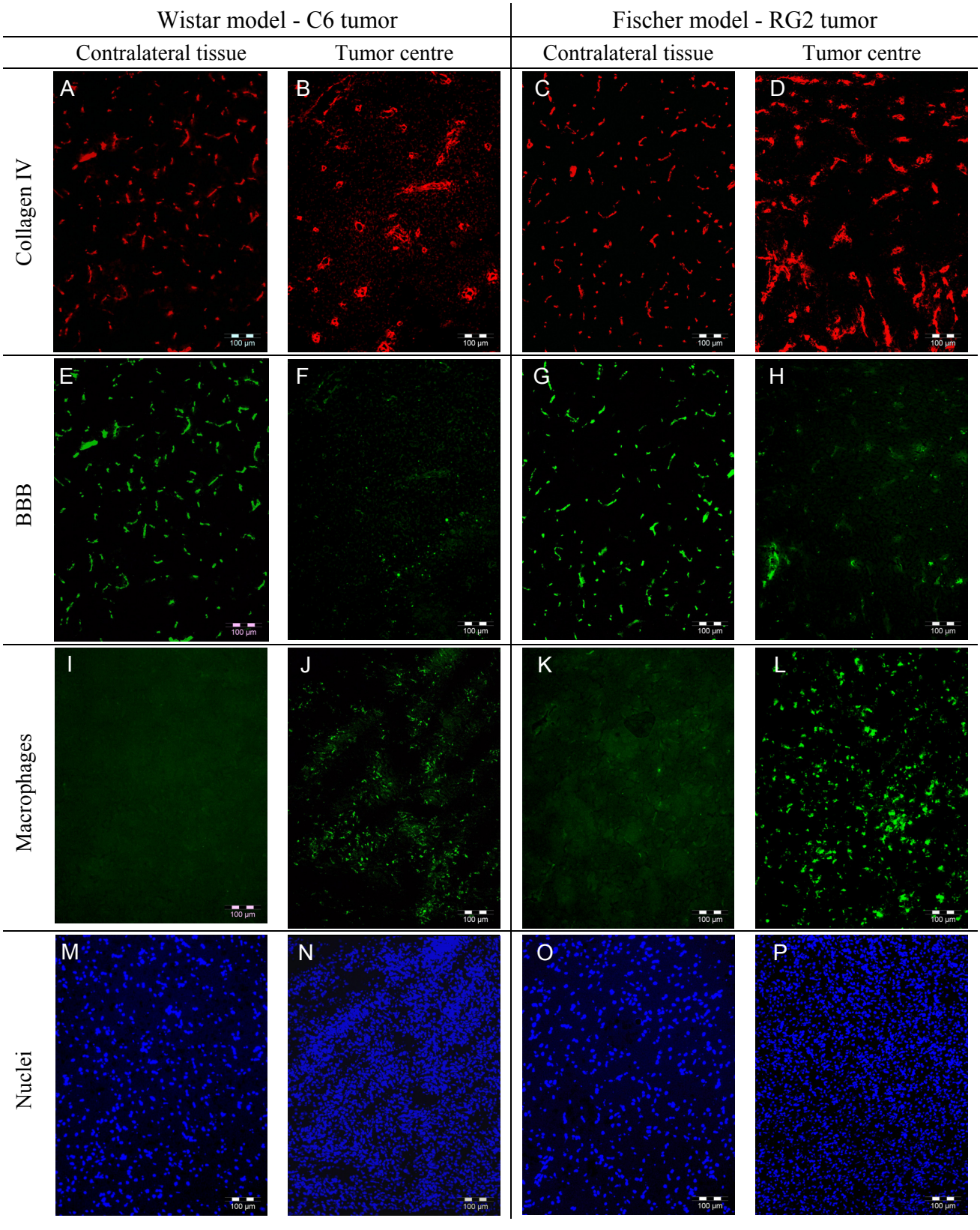
Examples of histological images obtained for the C6 model (two left columns) and the RG2 model (two right columns). For each model, the tumor centre (right) and the contralateral region are represented (left). **(A-D)** Collagen IV staining, **(E-H)** BBB staining, **(I-L)** macrophage staining and **(M-P)** nucleus staining. Collagen IV and BBB stainings were performed on the same slice as well as macrophage and nucleus stainings.

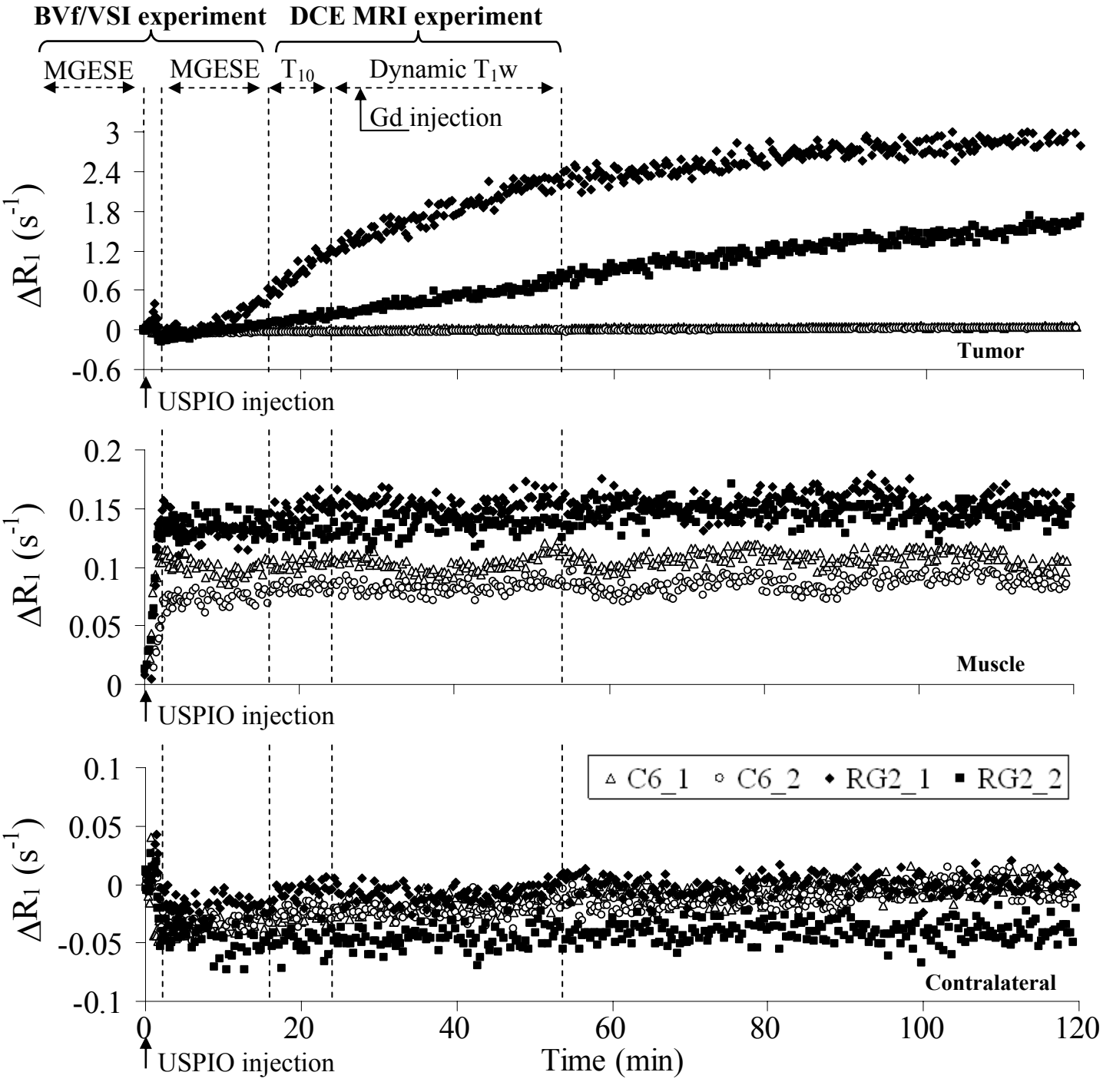
Table 1: DCE MRI pharmacokinetic parameter estimates, obtained in presence or in absence of USPIO, and BVf and VSI estimates, obtained from MRI data and histological data, for C6 and RG2 models.

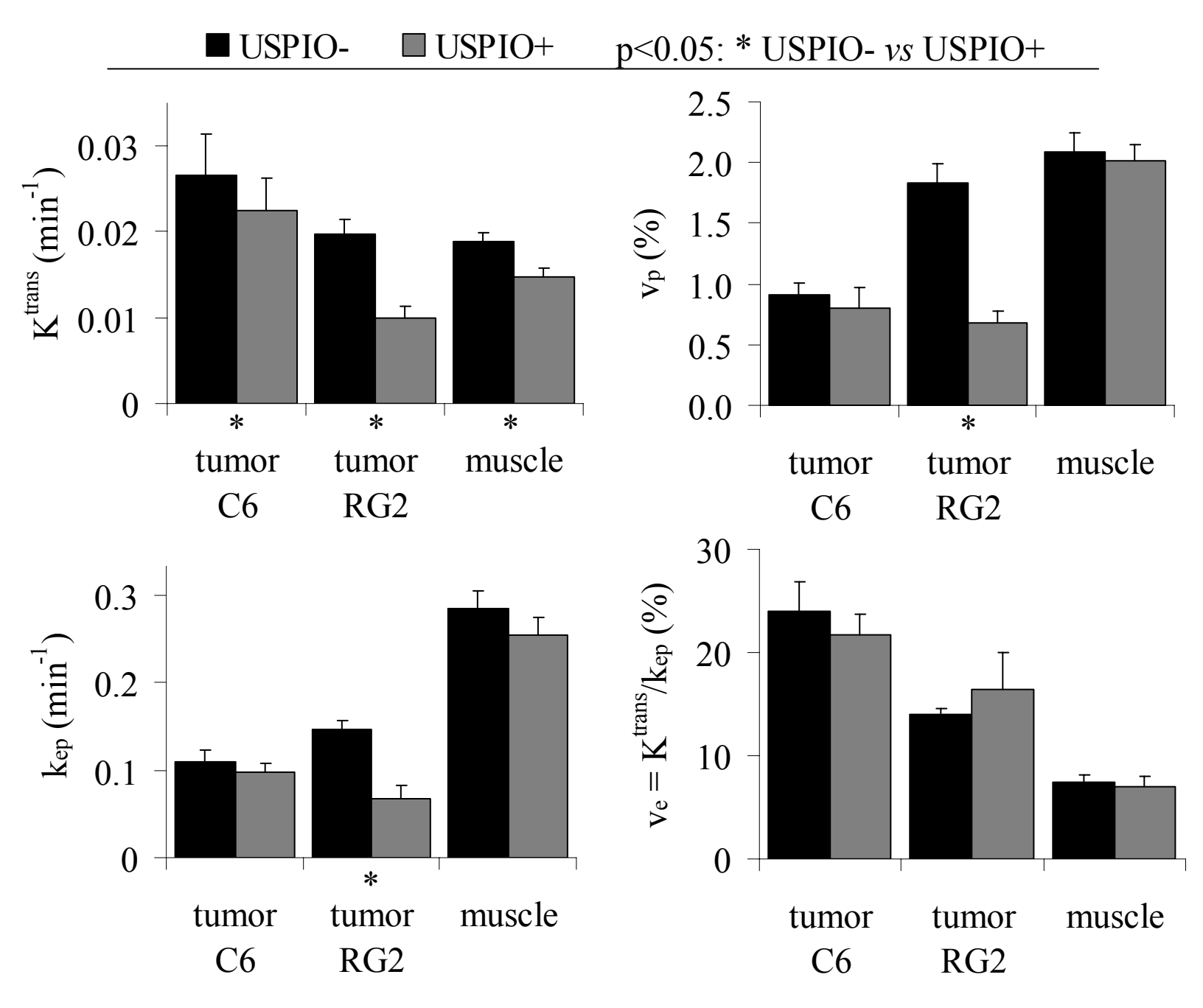
The pharmacokinetic parameters obtained in Session 1 (USPIO-) and in Session 2 (USPIO+) are reported in this table as mean±SEM as well as the results of the statistical tests for the comparison C6 *versus* RG2, tumor *versus* muscle and USPIO- *versus* USPIO+. Data obtained in the muscle have been pooled across tumor models (n=20) while data from the C6 tumor and the RG2 tumor were kept separate (n=14 and n=6 respectively). BVf and VSI estimates obtained from MRI data and from histological data (BVf_{histo} and VSI_{histo}) are also reported as mean±SEM, as well as the statistical results of the comparison C6 *versus* RG2 and tumor *versus* contralateral.

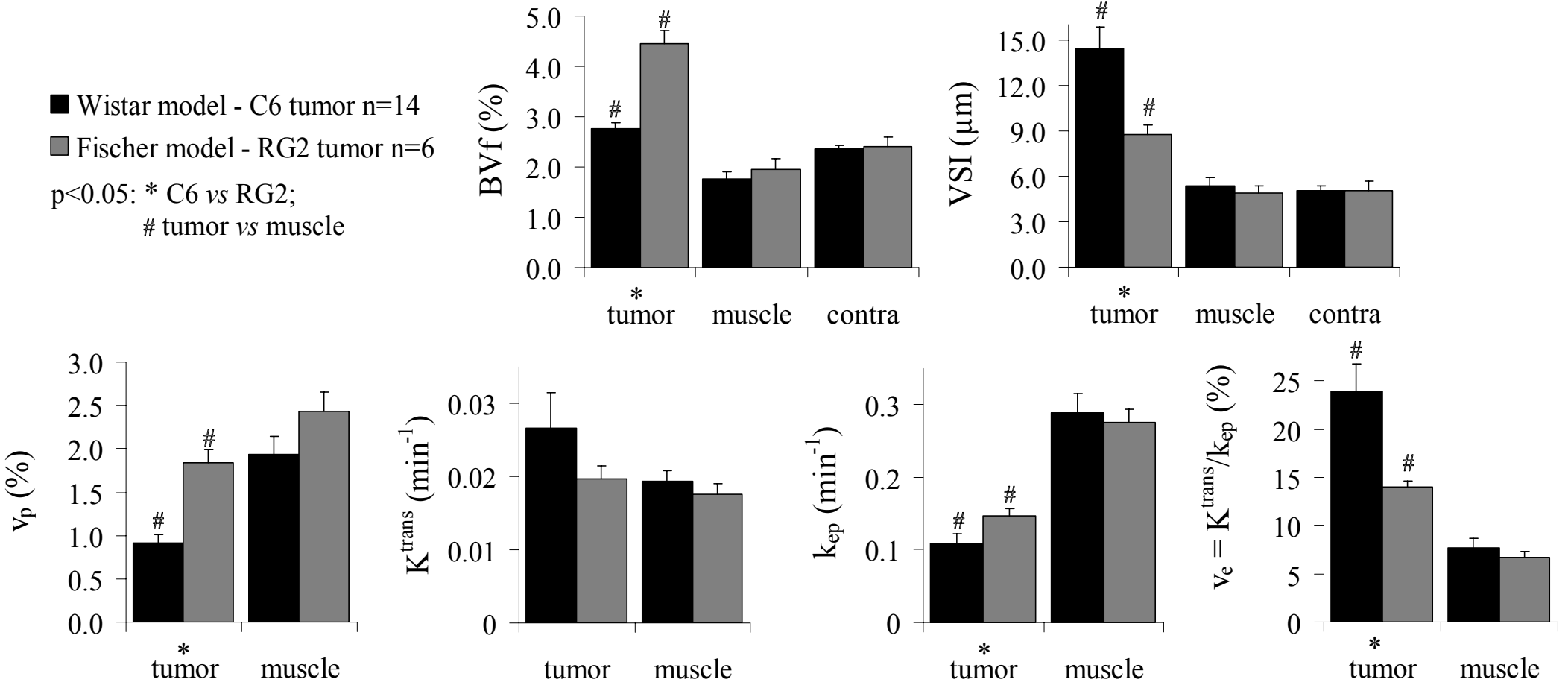
Parameters	Units	C6 tumor	RG2 tumor	Muscle	Contra	p-value		
DCE MRI / USPIO -		n = 14	n = 6	n = 20		C6 *versus* RG2	C6 *versus* Muscle	RG2 *versus* Muscle
v_p	%	0.9 ± 0.1	1.8 ± 0.2	2.1 ± 0.2	-	**$<10^{-3}$**	**$<10^{-3}$**	**0.016**
K^{trans}	10^{-2} min^{-1}	2.7 ± 0.5	2.0 ± 0.2	1.9 ± 0.1	-	0.203	0.096	0.156
k_{ep}	10^{-1} min^{-1}	1.1 ± 0.1	1.5 ± 0.1	2.8 ± 0.2	-	**0.042**	**$<10^{-3}$**	**0.016**
$v_e = K^{trans}/k_{ep}$	%	24.0 ± 2.9	13.9 ± 0.6	7.4 ± 0.7	-	**0.003**	**$<10^{-3}$**	**0.016**
DCE MRI / USPIO+		n = 14	n = 6	n = 20	n = 20	C6: USPIO- *versus* USPIO+	RG2: USPIO- *versus* USPIO+	Muscle: USPIO- *versus* USPIO+
v_p	%	0.8 ± 0.2	0.7 ± 0.1	2.0 ± 0.1	-	0.257	**0.016**	**0.016**
K^{trans}	10^{-2} min^{-1}	2.2 ± 0.4	1.0 ± 0.1	1.5 ± 0.1	-	**0.029**	**0.016**	**0.016**
k_{ep}	10^{-1} min^{-1}	1.0 ± 0.1	0.7 ± 0.2	2.5 ± 0.2	-	0.150	**0.016**	**0.016**
$v_e = K^{trans}/k_{ep}$	%	21.7 ± 2.0	16.4 ± 3.5	7.1 ± 0.9	-	0.134	0.250	0.250
BVf/VSI MRI		n = 14	n = 6	n = 20	n = 20	C6 *versus* RG2	C6 *versus* Muscle	RG2 *versus* Muscle
BVf	%	2.8 ± 0.1	4.5 ± 0.3	1.8 ± 0.1	2.4 ± 0.1	**$<10^{-3}$**	**$<10^{-3}$**	**0.016**
VSI	µm	14.4 ± 1.5	8.7 ± 0.7	5.2 ± 0.4	5.1 ± 0.3	**0.012**	**$<10^{-3}$**	**0.016**
Histology		n = 6	n = 5		n = 11	C6 *versus* RG2	C6 *versus* Contra	RG2 *versus* Contra
Vessel Density	vessels/mm^2	210 ± 94	261 ± 47	-	339 ± 89	0.156	**0.016**	**0.031**
BVf_{histo}	%	1.6 ± 0.6	3.7 ± 1.1	-	1.4 ± 0.2	**0.003**	0.093	**0.031**
VSI_{histo}	µm	5.4 ± 1.5	5.7 ± 0.6	-	3.4 ± 0.6	0.397	**0.016**	**0.031**

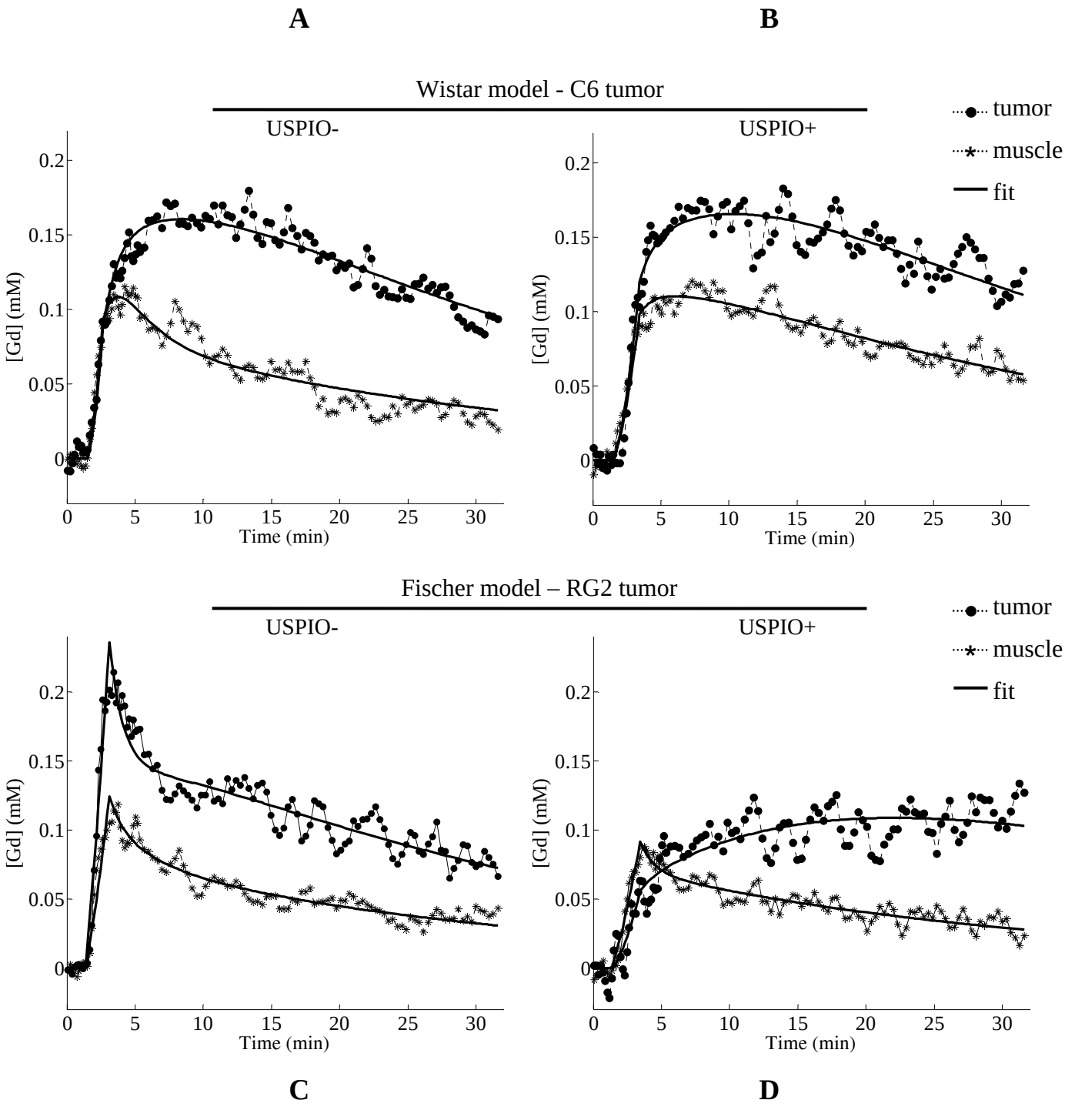
All statistical tests are paired permutation tests except C6 *versus* RG2, which is an unpaired permutation test.

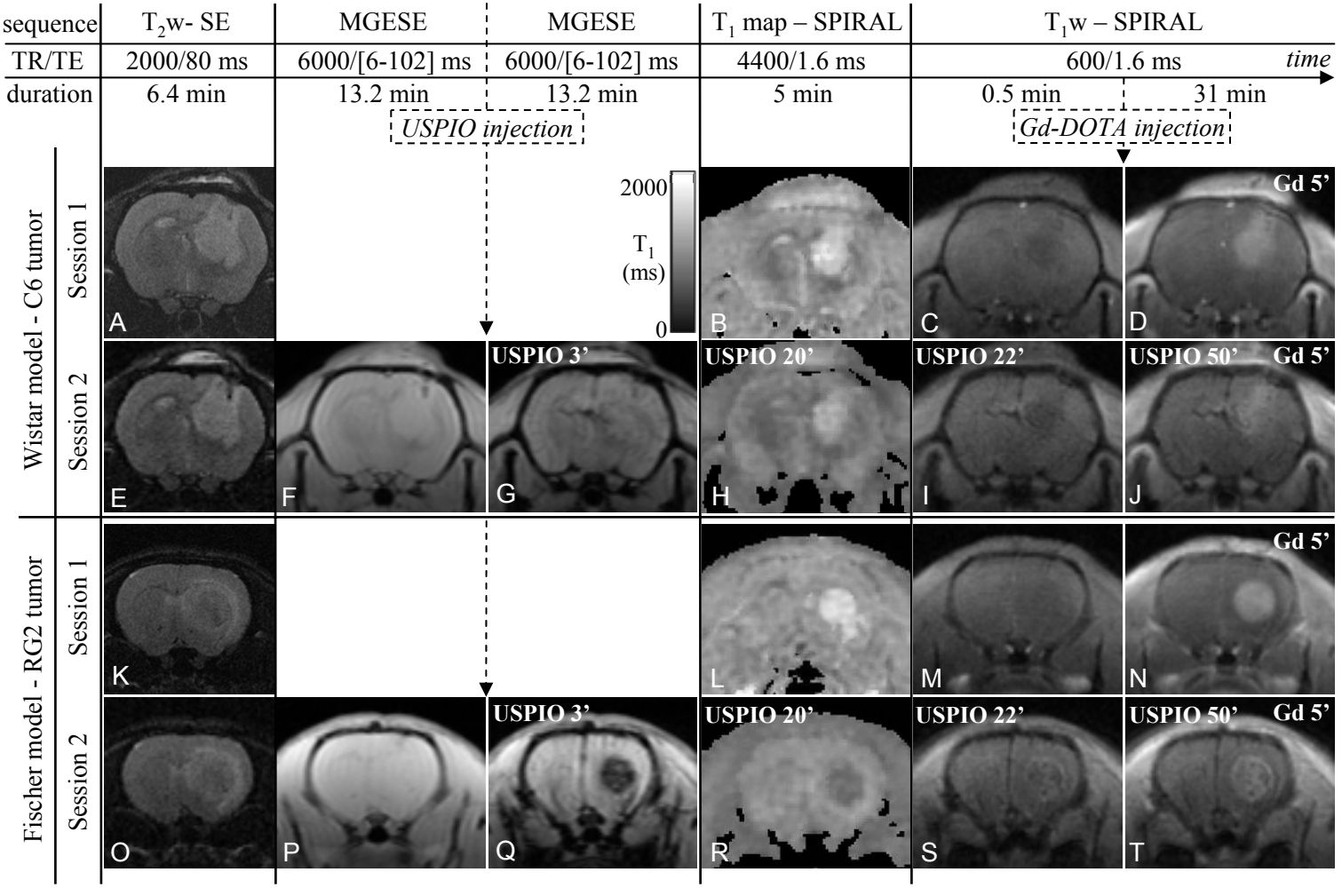

Wistar model - C6 tumor
Fischer model - RG2 tumor
Contralateral tissue
Tumor centre
Contralateral tissue
Tumor centre
Collagen IV
BBB
Macrophages
Nuclei
A
B
C
D
E
F
G
H
I
J
K
L
M
N
O
P
100 µm


BVf/VSI experiment
DCE MRI experiment
MGESE
MGESE
T_{10}
Dynamic T_1w
Gd injection
ΔR_1 (s^{-1})
3
2.4
1.8
1.2
0.6
0
-0.6
Tumor
USPIO injection
0.2
0.15
0.1
0.05
0
Muscle
USPIO injection
0.1
0.05
0
-0.05
-0.1
C6_1
C6_2
RG2_1
RG2_2
Contralateral
0
20
40
60
80
100
120
USPIO injection
Time (min)


USPIO-
USPIO+
p<0.05: * USPIO- vs USPIO+
K^{trans} (min^{-1})
0.03
0.02
0.01
0
*
*
*
tumor C6
tumor RG2
muscle
v_p (%)
2.5
2.0
1.5
1.0
0.5
0.0
*
tumor C6
tumor RG2
muscle
k_{ep} (min^{-1})
0.3
0.2
0.1
0
*
tumor C6
tumor RG2
muscle
$v_e = K^{trans}/k_{ep}$ (%)
30
20
10
0
tumor C6
tumor RG2
muscle


Wistar model - C6 tumor n=14
Fischer model - RG2 tumor n=6
p<0.05: * C6 vs RG2;
tumor vs muscle
BVf (%)
5.0
4.0
3.0
2.0
1.0
0.0
#
#
*
tumor
muscle
contra
VSI (µm)
15.0
12.0
9.0
6.0
3.0
0.0
#
#
*
tumor
muscle
contra
v_p (%)
3.0
2.5
2.0
1.5
1.0
0.5
0.0
#
#
*
tumor
muscle
K^{trans} (min^{-1})
0.03
0.02
0.01
0
tumor
muscle
k_{ep} (min^{-1})
0.3
0.2
0.1
0
#
#
*
tumor
muscle
$v_e = K^{trans}/k_{ep}$ (%)
25
20
15
10
5
0
#
#
*
tumor
muscle


A
B
Wistar model - C6 tumor
USPIO-
USPIO+
tumor
muscle
fit
[Gd] (mM)
Time (min)
Fischer model – RG2 tumor
C
D


sequence
T_2w- SE
MGESE
MGESE
T_1 map – SPIRAL
T_1w – SPIRAL
TR/TE
2000/80 ms
6000/[6-102] ms
6000/[6-102] ms
4400/1.6 ms
600/1.6 ms
time
duration
6.4 min
13.2 min
13.2 min
5 min
0.5 min
31 min
USPIO injection
Gd-DOTA injection
2000
T_1 (ms)
0
Wistar model - C6 tumor
Session 1
Session 2
Fischer model - RG2 tumor
Session 1
Session 2
A
B
C
D
E
F
G
H
I
J
K
L
M
N
O
P
Q
R
S
T
Gd 5'
USPIO 3'
USPIO 20'
USPIO 22'
USPIO 50'
Gd 5'
USPIO 3'
USPIO 20'
USPIO 22'
USPIO 50'
Gd 5'